Investigation of Biotransport in a Tumor With Uncertain Material Properties Using a Nonintrusive Spectral Uncertainty Quantification Method

Alen Alexanderian
Department of Mathematics,
North Carolina State University,
Raleigh, NC 27695
e-mail: alexanderian@ncsu.edu

Liang Zhu
Department of Mechanical Engineering,
University of Maryland, Baltimore County,
Baltimore, MD 21250

Maher Salloum
Extreme Scale Data Science and Analytics,
Sandia National Labs,
Livermore, CA 94550

Ronghui Ma
Department of Mechanical Engineering,
University of Maryland, Baltimore County,
Baltimore, MD 21250

Meilin Yu
Department of Mechanical Engineering,
University of Maryland, Baltimore County,
Baltimore, MD 21250
e-mail: mlyu@umbc.edu

In this study, statistical models are developed for modeling uncertain heterogeneous permeability and porosity in tumors, and the resulting uncertainties in pressure and velocity fields during an intratumoral injection are quantified using a nonintrusive spectral uncertainty quantification (UQ) method. Specifically, the uncertain permeability is modeled as a log-Gaussian random field, represented using a truncated Karhunen–Lòeve (KL) expansion, and the uncertain porosity is modeled as a log-normal random variable. The efficacy of the developed statistical models is validated by simulating the concentration fields with permeability and porosity of different uncertainty levels. The irregularity in the concentration field bears reasonable visual agreement with that in MicroCT images from experiments. The pressure and velocity fields are represented using polynomial chaos (PC) expansions to enable efficient computation of their statistical properties. The coefficients in the PC expansion are computed using a nonintrusive spectral projection method with the Smolyak sparse quadrature. The developed UQ approach is then used to quantify the uncertainties in the random pressure and velocity fields. A global sensitivity analysis is also performed to assess the contribution of individual KL modes of the log-permeability field to the total variance of the pressure field. It is demonstrated that the developed UQ approach can effectively quantify the flow uncertainties induced by uncertain material properties of the tumor. [DOI: 10.1115/1.4037102]

Keywords: uncertain permeability and porosity, statistical modeling, mass transportation, uncertainty quantification, Karhunen–Lòeve expansion, polynomial chaos, nonintrusive spectral projection, sparse quadrature

1 Introduction

Modeling drug transport in tissues has recently gained much attention in the bioengineering community due to its vast areas of applications [1], e.g., targeted drug delivery with nanomedicine [2] and hyperthermia with nanoparticles [3]. Intravenous injection is perhaps the most widely used method to administer drugs in a tumor. In this case, the organ usually needs to have well-defined supplying vessels such as those in liver or kidney. Intratumoral infusion is an alternative approach to deliver nanoparticles into the extracellular space in tumors in clinical study [4–8]. This approach addresses the limitations of vascular particle delivery and does not depend on tumor vasculature. Positive pressure infusion is often employed in intratumoral infusion to directly inject nanoparticles into the target tissue. This process is often referred to as convection enhanced delivery. There are many studies that address this problem in the literature [9]. These studies rely on mathematical models of flow in porous media (e.g., Darcy and Brinkman) and are successful in accounting for the existence of capillaries, tissue metabolism, etc. However, these mathematical models rely on the assumption that the tissue properties (e.g., permeability) are uniform. MicroCT imaging following nanofluid infusion [3] often reveals highly irregular nanoparticle distributions in tumors due to the spatial heterogeneity of the tissue (see two images from MicroCT imaging of the distribution of nanoparticles in tumors after injection as shown in Fig. 1). As a matter of fact, the microstructure of tumors is usually heterogeneous. Several previous works [10–14] have studied biomass/heat transfer in tumors with heterogeneous material properties. However, the structural heterogeneity used in previous studies is usually a deterministic property of a specific tumor. This approach cannot account for randomness of material properties in tumors. Thus, the results do not reflect statistical trend, which can provide insight in cancer therapy design. Therefore, it is of clinical significance to model biomass/heat transfer with quantified uncertainties resulting from the structural randomness in tissues.

As discussed, previous theoretical simulations of biotransport in porous media usually model a tumor as a structure with uniform

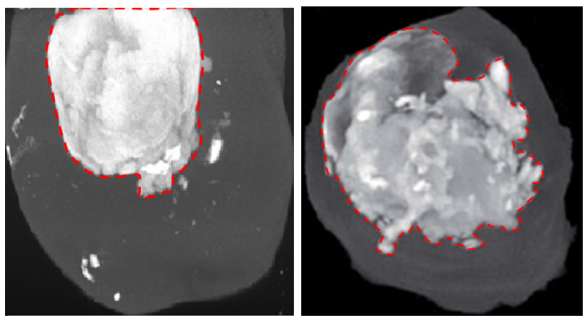

Fig. 1 MicroCT images of nanoparticle distribution (bright regions enclosed by the dash lines) in two tumors (grey regions): (*a*) regular nanoparticle distribution and (*b*) irregular nanoparticle distribution

Manuscript received February 3, 2017; final manuscript received May 16, 2017; published online July 14, 2017. Assoc. Editor: Ram Devireddy.

or deterministic heterogeneous transport properties. In contrast, in this work, statistical models will be developed to approximate material properties of tumors. Spectral uncertainty quantification (UQ) methods will be used to quantify the impact of material heterogeneities on the mass transport process in tumors. In particular, a spectral UQ approach based on polynomial chaos (PC) expansions is used to investigate the effect of random permeability on the pressure and interstitial velocity. Generally, there are two ways to compute PC expansions: (1) the intrusive approach [15–21] and (2) the nonintrusive approach [21–24]. The latter is the approach used in the present work. A nonintrusive UQ approach provides excellent flexibility in resolving practical complex thermal fluids problems. Specifically, in this approach, no modification is needed for the available deterministic simulation tools. This can take full advantage of the contemporary development of high-fidelity computational fluid dynamics methods. In the present work, a nonintrusive spectral projection approach, utilizing Smolyak sparse quadrature [25], is used to compute the PC coefficients of the quantities of interest. The information collected from this study can be used to study concentration field in biological systems with uncertain permeability and porosity.

We note that most previous uncertainty analyses of the biomass/heat transfer process were based on perturbation analysis [26,27] or Monte Carlo (MC) methods [28,29]. Although a large amount of simulations can guarantee that MC achieves convergence, the computational cost is usually prohibitive, especially for intricate flow problems. In contrast, an UQ approach based on PC expansions, as developed in the current study, provides an efficient modeling framework to quantify the uncertainty in a complicated problem. A similar UQ approach but with the intrusive spectral projection method has been adopted by other researchers [30,31] to analyze geophysical flow in porous media. To the best of the authors' knowledge, this study is the first attempt to systematically model the uncertain heterogeneous tumor structure as a random process and to quantify the uncertainties in pressure and velocity fields using a nonintrusive PC approach.

The remainder of the paper is organized as follows: The mathematical models, including the Darcy's law constrained by mass conservation, the convection equations of concentration, and the model parameters, are introduced in Sec. 2. In Sec. 3, the statistical models for uncertain permeability and porosity are presented. Specifically, the uncertain permeability is modeled as a log-Gaussian random field, and a truncated Karhunen–Lòeve (KL) expansion is used to control its dimension. The uncertain porosity is modeled as a log-normal random variable. Propagating these statistical models through the governing partial differential equations (PDEs) will result in random pressure, velocity, and concentration fields. A full investigation of the uncertain nature of the time-dependent concentration field, which can be directly measured in experiments, is the ultimate goal of our research. As a first step, a brief illustration of uncertainties in concentration field is provided at the end of Sec. 3, which also demonstrates the efficacy of the developed statistical models. To quantify the uncertainties in the time-dependent concentration field, we need to have a complete understanding of how material uncertainties affect pressure and velocity fields, the uncertainty of which will be further propagated into the concentration fields. Therefore, a major focus of this work is to quantify the uncertainties in pressure and velocity fields using PC expansions, which is elaborated in Sec. 4. Numerical results are presented and discussed in Sec. 5. A global sensitivity analysis [24,32–35] is also performed for the pressure field in the same section. Section 6 concludes this study.

2 Mathematical Model

The pressure, velocity, and concentration fields in a spherical tumor are simulated when single-needle injection occurs at the tumor center. Consider the Darcy's law constrained by mass conservation in the spherical coordinate system

$$\nabla \cdot \left(\frac{\kappa}{\mu}\nabla P\right) = 0, \quad \nabla = \frac{\partial}{\partial r}\mathbf{e}_r + \frac{1}{r}\frac{\partial}{\partial \theta}\mathbf{e}_\theta + \frac{1}{r\sin\theta}\frac{\partial}{\partial \varphi}\mathbf{e}_\varphi \tag{1}$$

where P is the pressure, κ is the permeability, μ is the fluid dynamic viscosity, r is the radial distance from a fixed origin, and θ and φ are the polar and azimuth angles, respectively. In the current study, a two-dimensional model in the (r, φ) plane with a fixed polar angle $\theta = \pi/2$ is used. As a result, the governing equation for the pressure P is written as

$$\frac{\partial}{\partial r}\left(\frac{\kappa r^2}{\mu}\frac{\partial P}{\partial r}\right) + \frac{\partial}{\partial \varphi}\left(\frac{\kappa}{\mu}\frac{\partial P}{\partial \varphi}\right) = 0 \tag{2}$$

The two-dimensional physical domain, represented using (r, φ) coordinates, is

$$D = \{(r, \varphi): R_{\text{needle}} < r < R_{\text{tumor}},\ 0 < \varphi < 2\pi\}$$

Herein, R_{tumor} is the radius of the tumor and R_{needle} is the radius of the needle, which is used to inject nanofluid into the tumor; see Fig. 2 (top) for a depiction of the computational domain. The boundary conditions for the pressure equation are specified as follows:

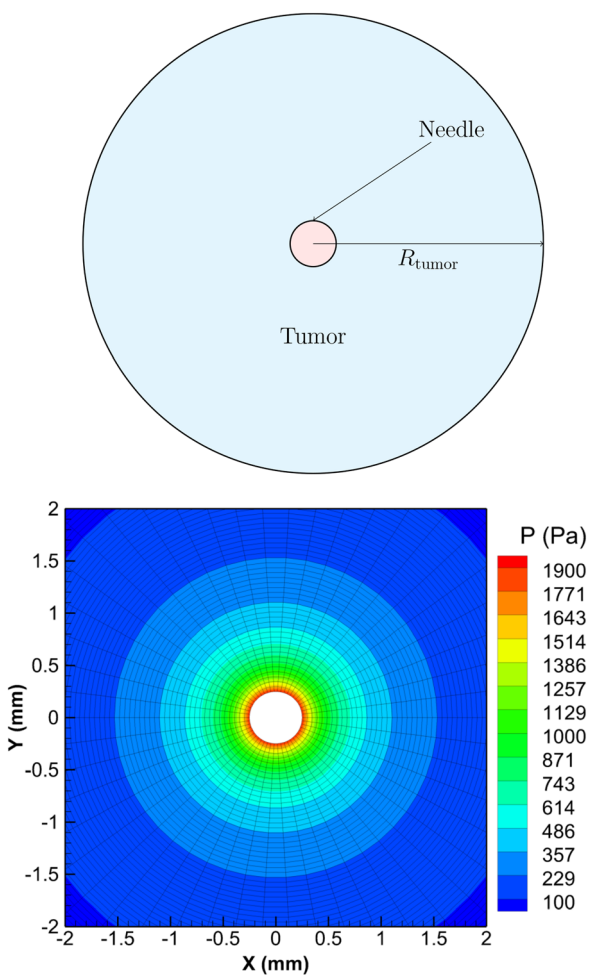

Fig. 2 Top the two-dimensional computational domain is given by a circle of radius R_{tumor} with the concentric inner circle of radius R_{needle} removed. This models a tumor with an injection site at the center; and bottom: the pressure field with constant material properties.

Table 1 Nominal values for the model parameters [36]

Parameters	Nominal value
Tumor permeability, κ	0.5 md
Tumor porosity, ϕ	0.2
Fluid viscosity, μ	8.9×10^{-4} Pa · s
Infusion rate, Q	1 μL/min
Needle radius, R_{needle}	0.25 mm
Tumor radius, R_{tumor}	5 mm

$$\begin{cases} p = 0, & r = R_{\text{tumor}} \\ \dfrac{\partial p}{\partial r} = \dfrac{-Q\mu}{4\pi R_{\text{needle}}^2 \kappa}, & r = R_{\text{needle}} \end{cases} \tag{3}$$

Note that to enforce mass conservation in the spherical coordinate system, $4\pi R_{\text{needle}}^2$ is used in the natural boundary condition Eq. (3) at $r = R_{\text{needle}}$. Periodic boundary condition is enforced in the φ direction.

The nanoparticle concentration field C is governed by the advection–diffusion equation

$$\frac{\partial C}{\partial t} + \nabla \cdot (\mathbf{v}C) = \nabla \cdot (D_e \nabla C) - k_f C \tag{4}$$

Here, D_e is the effective diffusion coefficient, k_f is the deposition rate coefficient, and $\mathbf{v}$ is the interstitial velocity in the flow field, which by Darcy's law is given by

$$\mathbf{v} = -\frac{\kappa}{\phi\mu}\nabla P$$

where ϕ is the porosity. The initial and boundary conditions are defined as follows:

$$\begin{cases} C(t = 0, r \neq R_{\text{needle}}, \varphi) = 0 \\ C(t, r = R_{\text{needle}}, \varphi) = 1 \\ \dfrac{\partial C}{\partial r}(t, r = R_{\text{tumor}}, \varphi) = 0 \end{cases} \tag{5}$$

Periodic boundary condition is enforced in the φ direction.

The second-order accurate central finite difference scheme is used to discretize the pressure Eq. (2), and an implicit Gauss–Seidel method in the r-direction is used to solve the resulting discrete system. In our computations, we ensure that the absolute residual is reduced to below 10^{-8}. In Fig. 2 (bottom), we report the pressure field computed by solving the equation with parameters as specified in Table 1, over the discretized computational domain. The convection term of the concentration Eq. (4) is discretized with the second-order upwind scheme, and the equation is marched in the temporal direction using the explicit two stage Runge–Kutta scheme.

3 Statistical Model for Uncertain Parameters

The tumor is a heterogeneous medium with uncertain material properties, namely, permeability and porosity. Below, we detail our modeling assumptions on the statistical properties of the permeability field, followed by the statistical model for uncertain porosity.

3.1 Uncertain Permeability Parameterization. The permeability field κ is modeled as a random field $\kappa = \kappa(\mathbf{x}, \omega)$, where $\mathbf{x}$ is a spatial point in D and ω belongs to an appropriate sample space. Specifically, we model κ by a log-Gaussian random field as follows: letting $a(\mathbf{x}, \omega) = \log(\kappa(\mathbf{x}, \omega))$, we assume

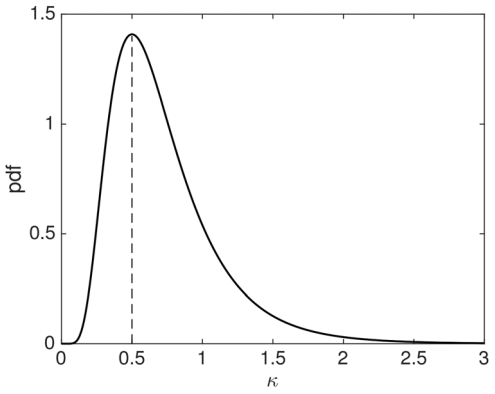

Fig. 3 Log-normal model for permeability values (at each spatial point in the tumor)

$$a(\mathbf{x}, \omega) = a_0 + z(\mathbf{x}, \omega) \tag{6}$$

Here, a_0 is the pointwise mean of the process and z is a centered (mean zero) Gaussian process with pointwise variance $\text{Var}\{z(\mathbf{x}, \cdot)\} = \sigma_a^2$, for every $\mathbf{x} \in D$. To fully specify the distribution law of a, we need to define a_0, σ_a, as well as the correlation structure of the Gaussian process z. First, we specify the values for a_0 and σ_a

$$\sigma_a^2 = 0.25, \quad a_0 = \log(0.5) + \sigma_a^2$$

The rationale behind the choice of a_0 is to ensure that the mode[1] of the κ distribution at each spatial point is $\exp(a_0 - \sigma_a^2) = 0.5$, which is the nominal value for κ given in Table 1. The selected value of σ_a^2 allows for reasonable variations of κ in a physically meaningful range. In Fig. 3, we depict the probability density function as a log-normal random variable, with these parameter choices to illustrate the distribution of κ at each spatial point.

Next, we specify the correlation structure of the stochastic log-permeability field. We assume z in Eq. (6) has a correlation function of the form

$$c(\mathbf{x}, \mathbf{y}) = \sigma_a^2 \exp\left\{-\frac{1}{\ell}||\mathbf{x} - \mathbf{y}||_2\right\}, \quad \mathbf{x}, \mathbf{y} \in D \tag{7}$$

where $\ell > 0$ controls the correlation length and, as before, D is the physical domain of the problem. Note that the covariance operator of the process z is the linear operator $C : L^2(D) \to L^2(D)$, defined by

$$[Cu](\mathbf{x}) = \int_D c(\mathbf{x}, \mathbf{y}) u(\mathbf{y})\, d\mathbf{y}, \quad u \in L^2(D)$$

Let $\{\lambda_i\}_{i \geq 1}$ be (real, non-negative) eigenvalues of C and $\{e_i\}_{i \geq 1}$ the corresponding eigenfunctions

$$\int_D c(\cdot, \mathbf{y}) e_i(\mathbf{y})\, d\mathbf{y} = \lambda_i e_i(\cdot), \quad i = 1, 2, 3, \ldots$$

In what follows, we use a truncated KL expansion (e.g., see Refs. [21] and [37]) to represent a

$$a(\mathbf{x}, \omega) \approx a_0(\mathbf{x}) + \sum_{k=1}^{N_{\text{KL}}} \sqrt{\lambda_k}\, \xi_k(\omega) e_k(\mathbf{x}) \tag{8}$$

[1]Consider a log-normal random variable $X = \exp(\mu + \sigma\xi)$, where ξ is a standard normal random variable, $\mu \in \mathbb{R}$, and $\sigma \in \mathbb{R}_+$. The mode of X is given by $\exp(\mu - \sigma^2)$.

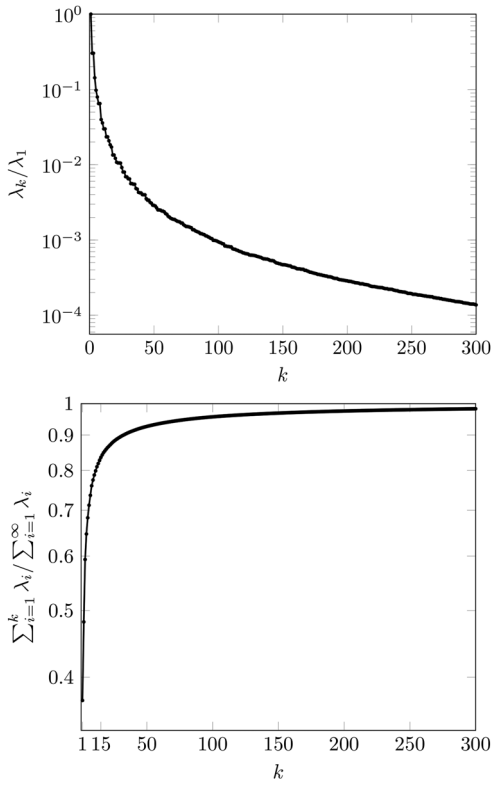

Fig. 4 The normalized eigenvalues (top) and the ratio $r_{N_{KL}}$ that quantifies variance saturation as a function of *n* (bottom), corresponding to correlation length $\ell = 5$ mm, which is the radius of the tumor model

where due to Gaussianity of the process, ξ_k are independent standard normal random variables. Note that in this formulation, the uncertainty in a (and hence κ) is characterized by $\boldsymbol{\xi} = (\xi_1, \xi_2, \ldots, \xi_{N_{KL}})$. Therefore, we use

$$\kappa(\mathbf{x}, \boldsymbol{\xi}) = \exp\left(a_0(\mathbf{x}) + \sum_{k=1}^{N_{KL}} \sqrt{\lambda_k}\xi_k e_k(\mathbf{x})\right) \tag{9}$$

as the statistical model for the uncertain permeability field.

The truncation of the KL expansion of the Gaussian process $a(\mathbf{x}, \omega)$ is traditionally done by choosing N_{KL} such that

$$r_{N_{KL}} = \frac{\sum_{k=1}^{N_{KL}} \lambda_k}{\sum_{k=1}^{\infty} \lambda_k} < \text{tol} \tag{10}$$

where tol is a user-specified tolerance. Note that computing the denominator in Eq. (10) is straightforward in the present setup and does not require computing all the eigenvalues. We know by Mercer's Theorem [38] that

$$\int_D c(\mathbf{x}, \mathbf{x})\, d\mathbf{x} = \text{Tr}(C) = \sum_{k=1}^{\infty} \lambda_k$$

Thus, with our choice of covariance function (7), $\int_D c(\mathbf{x}, \mathbf{x})\, d\mathbf{x} = \sigma_a^2 \text{vol}(D)$. Therefore, $\sum_{k=1}^{\infty} \lambda_k = \sigma_a^2 \text{vol}(D)$. In Fig. 4, we report the normalized eigenvalues of the covariance operator (left) and the ratio $r_{N_{KL}}$ (right).

In Fig. 5 (top row), we show two realizations of the log-permeability field with correlation length $\ell = 5$mm. For each realization, we solve the pressure equation and report the resulting pressure field (Pa) in Fig. 5 (bottom row). In the results reported in Fig. 5, we used a truncated KL expansion with $N_{KL} = 15$ modes. Note that with $n = 15$ modes, we have $r_{N_{KL}} \approx 0.86$, indicating that 86% of variance is captured by letting $N_{KL} = 15$. It is also important to note that while the higher order KL truncations provide more accurate representation of the random field, the governing PDE, which is the Poisson pressure equation in this case, has a smoothing solution operator that is not very sensitivity to the higher order, highly oscillatory, modes of the parameter. This is quantified in Sec. 5 by performing a sensitivity analysis of the pressure field with respect to the KL modes.

3.2 Uncertain Porosity Parameterization. Following the development in Ref. [31], we model the porosity by a scalar-valued random variable. Specifically, we assume a log-normal distribution for ϕ

$$\phi = \exp(b(\eta)), \quad b(\eta) = b_0 + \sigma_b \eta \tag{11}$$

where η is a standard normal random variable, and b_0 and σ_b are the mean and standard deviation of log-porosity, respectively. We use $\sigma_b^2 = 0.25$ and $b_0 = \log(0.2) + \sigma_b^2$. With these parameter choices, the mode of the porosity distribution coincides with its nominal value given in Table 1, and a reasonably wide range of values lie in the high-probability region of the distribution.

Using the aforementioned parameterization, we get the following representation for the uncertain interstitial velocity:

$$\mathbf{v}(\mathbf{x}, \boldsymbol{\xi}, \eta) = -\frac{\kappa(\mathbf{x}, \boldsymbol{\xi})}{\phi(\eta)\mu} \nabla P(\mathbf{x}, \boldsymbol{\xi}) \tag{12}$$

The uncertainty in the velocity field then propagates in the advection–diffusion equation and leads to a stochastic concentration field $C = C(\mathbf{x}, \boldsymbol{\xi}, \eta)$.

3.3 Impact of Uncertainties in Material Properties on Drug Transport. Predictions obtained by simulating the governing PDEs should account of the uncertainties in material properties. This requires propagating the statistical model for material properties through the governing equations. In the present problem, the statistical model for permeability field enters the Poisson pressure equation (2), whose solution is the (uncertain) pressure field $P(\mathbf{x}, \boldsymbol{\xi})$. Then, using the model for uncertain interstitial velocity (12), we can solve the concentration equation (4). Here, we demonstrate the efficacy of the statistical models by illustrating the uncertainties in the concentration field originated from the uncertain material properties.

We illustrate the impact of uncertainties in material properties on the concentration field by reporting two realizations of the concentration fields associated with permeability fields of different correlation lengths, namely, $\ell = 5$ mm, 2 mm, 1 mm, and 0.5 mm, at 10 min in Fig. 6. It is observed that as the correlation length in the correlation function decreases, the shape of the outer boundary becomes more and more irregular. This bears reasonable visual agreement with the MicroCT images from experiments as shown in Fig. 1, demonstrating the efficacy of the developed statistical models for the uncertain permeability and porosity. Note that the shape irregularity of the outer boundaries of concentration fields is used here for qualitative visual validation between numerical and experimental results. This is because that in experiments, nanoparticles are directly injected into the interstitial space of tumors; however, in numerical simulation, the tumors are modeled as porous media with porosity and permeability. Therefore, a point-to-point comparison between numerical and experimental results is not meaningful. Instead, we focus on the shape irregularity of the outer boundaries of concentration fields, which reflects the uncertainty in porosity and permeability, or equivalently, the uncertainty/heterogeneity in material properties of tumors used in experiments.

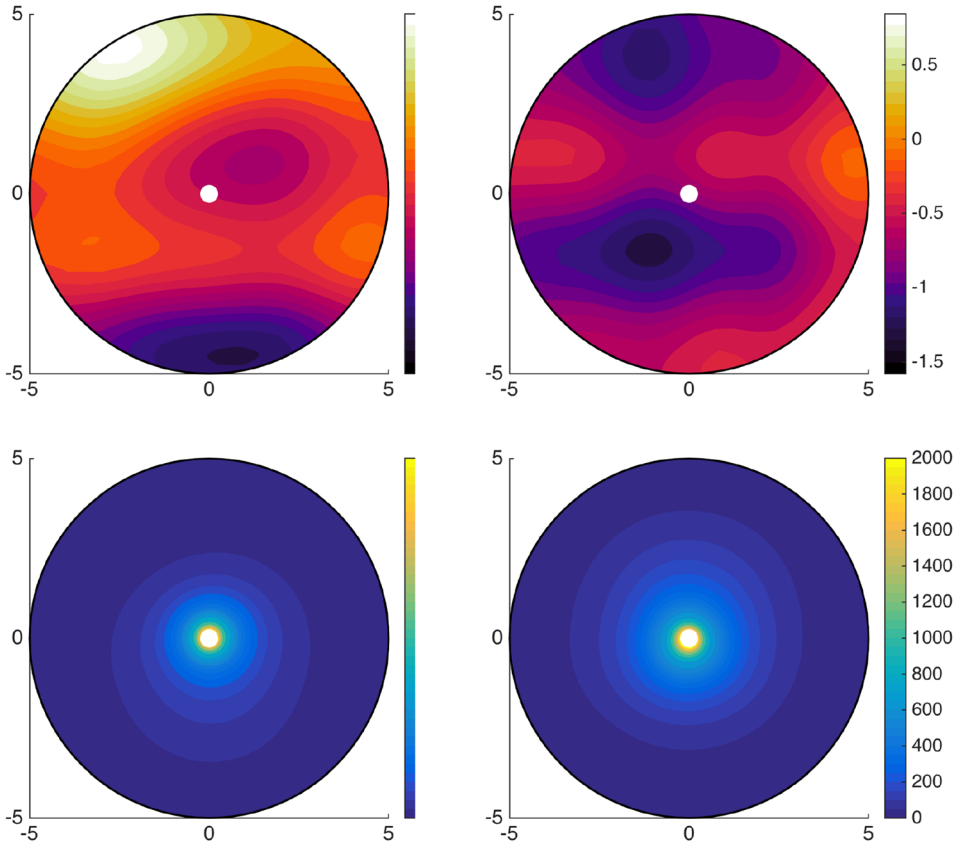

Fig. 5 Two realizations of the uncertain log-permeability field (top) and the corresponding pressure fields (bottom)

The full investigation of uncertainties in concentration field can be divided into two subtasks: (1) understanding the impact of uncertainties in material properties on pressure field and pressure gradient and (2) developing a statistical framework for understanding the uncertainties in concentration field. This paper is focused on the first task. In the following, we utilize an efficient computational framework based on PC expansions for characterizing the uncertainties in pressure field (and subsequently pressure gradient and interstitial velocity).

4 Polynomial Chaos for Representing Uncertain Pressure Field

We represent the model observables using polynomial chaos (PC) expansions [21,37,39]. PC expansions are series expansion of random variables in a multivariate orthogonal polynomial basis. For example, we represent the pressure field as

$$P(\mathbf{x},\boldsymbol{\xi}) \approx \sum_{k=0}^{N_{\mathrm{PC}}} c_k(\mathbf{x})\Psi_k(\boldsymbol{\xi}) \tag{13}$$

where Ψ_k's are appropriately chosen orthogonal polynomials and c_k's are expansion coefficients. Since in the present work $\boldsymbol{\xi}$ is a d-dimensional Gaussian random vector, we choose d-variate Hermite polynomials for $\{\Psi_k\}_{k=0}^{N_{\mathrm{PC}}}$. More precisely, if we denote by $\{\psi_j(\xi_i)\}_{j=1}^{\infty}$ the univariate Hermite polynomial basis corresponding to ξ_i, we form the multivariate PC basis functions as follows:

$$\Psi_k(\boldsymbol{\xi}) = \prod_{i=1}^{d} \psi_{\alpha_i^k}(\xi_i), \quad k = 0,1,2,\ldots \tag{14}$$

where $\alpha^k = (\alpha_1^k, \alpha_2^k, \ldots, \alpha_d^k)$ is a multi-index and d is the dimension of the random variable. With this notation, $\psi_{\alpha_i^k}$ is the Hermite polynomial of order α_i^k. The truncation of the PC expansion can be done in different ways. We choose total-order truncation [21], resulting in a complete polynomial space, in which case

$$N_{\mathrm{PC}} + 1 = \frac{(p+d)!}{p!d!} \tag{15}$$

where p is the maximum total polynomial degree. We note that another simple way to construct $\Psi_k(\boldsymbol{\xi})$'s is to use a full tensor product approach, in which case, $N_{\mathrm{PC}} + 1 = (p+1)^d$, which is much larger than N_{PC} in Eq. (15). For example, for $p = 3$ and $d = 15$, we get $N_{\mathrm{PC}} = 816$, if the complete polynomial space is used; while $N_{\mathrm{PC}} = 1,073,741,824$, if the full tensor product of univariate polynomials is used.

Once a PC expansion is available, statistical properties of P can be computed at negligible computational cost. For example, we have immediate access to the mean and variance of the pressure field through

$$\mathrm{E}(P(\mathbf{x},\boldsymbol{\xi})) = \langle P(\mathbf{x},\cdot), 1\rangle = c_0(\mathbf{x})$$

and

$$\begin{aligned}\mathrm{Var}(P(\mathbf{x},\boldsymbol{\xi})) &= \langle P(\mathbf{x},\cdot) - \mathrm{E}(P(\mathbf{x},\cdot)), P(\mathbf{x},\cdot) - \mathrm{E}(P(\mathbf{x},\cdot))\rangle \\ &= \sum_{i=1}^{N_{\mathrm{PC}}} c_i^2(\mathbf{x})\langle \Psi_i, \Psi_i\rangle\end{aligned}$$

Note that these relations follow from orthogonality of $\{\Psi_k\}_{k=0}^{P}$, $\langle \Psi_k, \Psi_l\rangle = \delta_{kl}\langle \Psi_k, \Psi_k\rangle$, $k,l = 1,\ldots,P$, and the convention $\Psi_0 \equiv 1$.

Moreover, we can compute statistical distribution of P efficiently by sampling the PC expansion of P, instead of repeated expensive solutions of the high-resolution pressure equation.

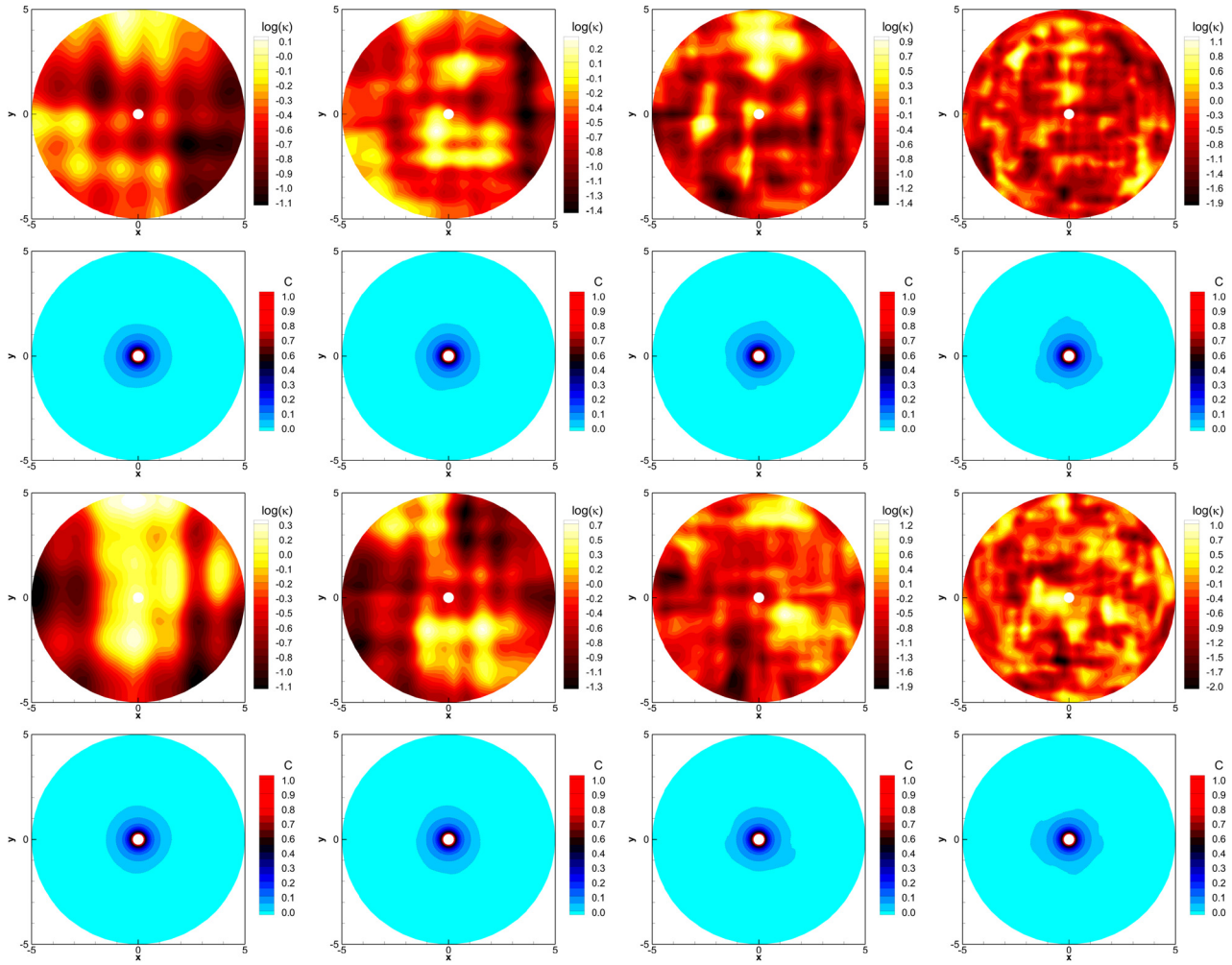

Fig. 6 Two sets of realizations of the uncertain log-permeability fields and the corresponding concentration fields at 10 mins. From left to right, the correlation lengths ℓ are 5 mm, 2 mm, 1 mm, and 0.5 mm, respectively.

4.1 Nonintrusive Spectral Projection. The PC expansion coefficients are evaluated via Galerkin projection; that is, we use

$$\begin{aligned}\langle P, \Psi_l \rangle &= \int P(\mathbf{x}, \boldsymbol{\xi}) \Psi_l(\boldsymbol{\xi}) \rho(\boldsymbol{\xi}) d\boldsymbol{\xi} \\ &= \sum_{k=0}^{N_{\text{PC}}} \int c_k(\mathbf{x}) \Psi_k(\boldsymbol{\xi}) \Psi_l(\boldsymbol{\xi}) \rho(\boldsymbol{\xi}) d\boldsymbol{\xi} \\ &= \sum_{k=0}^{N_{\text{PC}}} c_k(\mathbf{x}) \langle \Psi_k, \Psi_l \rangle = c_l(\mathbf{x}) \langle \Psi_l, \Psi_l \rangle\end{aligned} \tag{16}$$

where $\rho(\boldsymbol{\xi})$ is the probability density function corresponding to a d-dimensional standard normal distribution. In this study, numerical quadrature is used to calculate $\langle P, \Psi_l \rangle$ as

$$\langle P, \Psi_l \rangle \approx \sum_{i=1}^{N} P(\boldsymbol{\xi}^{(i)}) \Psi_l(\boldsymbol{\xi}^{(i)}) w_i \tag{17}$$

where $\boldsymbol{\xi}^{(i)}$ and w_i, $i = 1, \ldots, N$, are quadrature nodes and weights, respectively. This approach of computing spectral coefficients with quadrature is known as nonintrusive spectral projection.

4.2 The Choice of Quadrature Formula. The tensor product of univariate quadrature rules can be used in Eq. (17). This is expressed as follows:

$$\langle P, \Psi_l \rangle \approx \sum_{i_1=0}^{p} \cdots \sum_{i_d=0}^{p} P(\xi_{i_1}, \ldots, \xi_{i_d}) \Psi_l(\xi_{i_1}, \ldots, \xi_{i_d}) \prod_{k=1}^{d} w_{i_k} \tag{18}$$

Herein, a multi-index $\mathbf{i} = (i_1, \ldots, i_d)$ is introduced to indicate the position of quadrature points in the corresponding one-dimensional (1D) quadrature rules. As a result, ξ_{i_k} and w_{i_k}, $k = 1, \ldots, d$, are, respectively, the quadrature points and weights in the one-dimensional (1D) quadrature rules. Note that the computational cost of the numerical quadrature can be huge when the dimension is relatively large. For example, if p is selected as three, and d is selected as 15, the tensor product approach needs $(p+1)^d = 4^{15} = 1,073,741,824$ evaluations.

To temper the computational cost, we use the Smolyak sparse quadrature [25,40] to carry out the integration in Eq. (17). This procedure is briefly reviewed in the following; e.g., see Ref. [40] for more details.

As a first step, define the successive 1D univariate quadrature rules as $Q_{i_k}, i_k = 0, \ldots, p$ and $k = 1, \ldots, d$, with increasing accuracy. The difference of successive 1D operators is defined as

$$\Delta_{i_k=0} = Q_{i_k=0}, \quad \Delta_{i_k>0} = Q_{i_k} - Q_{i_k-1}, \quad k = 1, \ldots, d \tag{19}$$

As a result, the 1D quadrature of any variable V can be written as $Q_{i_k}[V] = \sum_{j=0}^{i_k} \Delta_j[V]$. With the multi-index $\mathbf{i} = (i_1, \ldots, i_d)$, a set $\mathbb{Z}_q^d$ for any integer q is defined as

$$\mathbb{Z}^d_{q<0} = \varnothing, \quad \mathbb{Z}^d_{q\geq 0} = \left\{ \mathbf{i} \in \mathbb{Z}^d : \sum_{k=1}^{d} i_k = d + q \right\} \tag{20}$$

where $\mathbb{Z}^d$ is the d-dimensional set of non-negative integers. The Smolyak sparse quadrature for any variable V with accuracy level $p+1$ can then be expressed as

$$A(d,p)[V] = \sum_{q=0}^{p} \sum_{\mathbf{i}\in\mathbb{Z}^d_q} (\Delta_{i_1} \otimes \cdots \otimes \Delta_{i_d})[V] \tag{21}$$

where $\otimes$ stands for the tensor product operation. Note that the Smolyak sparse quadrature rule can significantly alleviate the so-called "curse-of-dimension" caused by the full tensor product operation (18). For example, with the univariate Gaussian quadrature rule, a level four (i.e., $p=3$) Smolyak for a 15-dimensional problem only needs 5021 evaluations [40] (comparing to 1,073,741,824 evaluations resulted from the full tensor product). We note that a quadrature rule with accuracy level k integrates complete polynomials of total degree $2k-1$ exactly. As observed from Eqs. (16), (18), and (21), to preserve discrete orthogonality when evaluating $\langle \Psi_i, \Psi_j \rangle$, the total degree of the integrand should not exceed $2p+1$. As a result, the total degree of the orthogonal polynomial $\Psi_i(\boldsymbol{\xi})$ should not exceed p, no matter full tensor product or Smolyak sparse grids are adopted for quadrature.

5 Numerical Results and Discussion

In this section, we present our numerical results analyzing the propagation of uncertainties in material properties to the pressure field and interstitial velocity.

5.1 Uncertainty Quantification of the Pressure Field. Here, we focus on understanding and quantifying the impact of uncertainties in material properties on the pressure field using its PC representation. We consider the correlation length in Eq. (7) to be $\ell = 5$ mm, which is the radius of the domain. Following the truncation strategy outlined in Sec. 3 (see also, Fig. 4), we retain 15 KL modes, in the KL expansion of the log-permeability field. We build a PC expansion for the pressure using a level four Smolyak in the 15-dimensional parameter space with 5021 quadrature nodes, which is suitable for computation of PC expansions of degree up to three. The accuracy of the PC representation is confirmed by testing convergence in distribution and in L^2 as the PC order increases.

5.1.1 Building the PC Model and Validation. We consider the pressure field over the whole computational domain and compute its PC expansions, $P(r,\varphi,\boldsymbol{\xi}) \approx \sum_{k=0}^{P} c_k(r,\varphi)\Psi_k(\boldsymbol{\xi})$. We begin our analysis by focusing on the average pressure at the injection site; i.e., we consider

$$P^{\text{needle}}(\boldsymbol{\xi}) = \int_0^{2\pi} P(r_{\text{needle}}, \varphi, \boldsymbol{\xi})\, d\varphi \tag{22}$$

Using the PC representation of the pressure field, we have

$$P^{\text{needle}}(\boldsymbol{\xi}) \approx \sum_{k=0}^{P} \left[\int_0^{2\pi} c_k(r_{\text{needle}}, \varphi)\, d\varphi \right] \Psi_k(\boldsymbol{\xi})$$

To test the convergence of this approximation, as we increase the PC order, we sample the aforementioned PC representation 10^5 times and generate approximate probability density functions of P^{needle} via kernel density estimation. These results are reported in Fig. 7 (left). We note that the distributions obtained from second- and third-order expansions are qualitatively close to one another, indicating that a third-order PC expansion might provide an adequate statistical model for the pressure field.

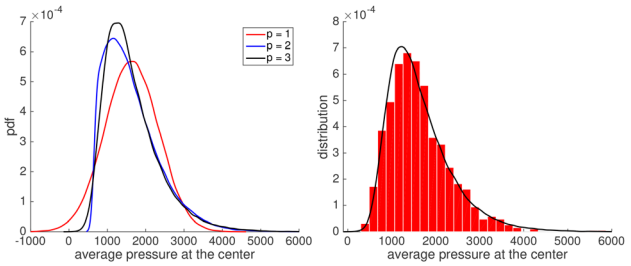

Fig. 7 Left: tracking the convergence of PDFs of the PC representation of P^{needle}; right: comparing the PDF of the third-order PC expansion of P^{needle} (solid line) with its empirical distribution generated through Monte Carlo sampling (histogram)

To enable a systematic test of the validity of the statistical model provided by the PC expansion, we generate a MC sample

$$\mathcal{S}_{\text{mc}} = \{\boldsymbol{\xi}_i\}_{i=1}^{N_{\text{mc}}}$$

with $N_{\text{mc}} = 1000$, and compute the pressure field $P(\mathbf{x}, \boldsymbol{\xi}_i)$, by solving the pressure equation, for $i = 1, \ldots, N_{\text{mc}}$. We compare the probability density function of third-order PC expansion of P^{needle} with the histogram of the P^{needle} model evaluations at the Monte Carlo points in Fig. 7 (right). We note that the distribution obtained using the PC model agrees well with the empirical distribution of P^{needle} constructed using Monte Carlo sampling.

To fully validate the accuracy of the PC model for the pressure field, we compute the following approximate relative L^2 error

$$E(r,\varphi) = \frac{\left[\sum_{j=1}^{N} \left(P(r,\varphi,\boldsymbol{\xi}_j) - \sum_{k=0}^{N_{\text{PC}}} c_k \Psi_k(\boldsymbol{\xi}_j) \right)^2 \right]^{1/2}}{\left[\sum_{j=1}^{N} P(r,\varphi,\boldsymbol{\xi}_j)^2 \right]^{1/2}}, \quad \boldsymbol{\xi}_j \in \mathcal{S}_{\text{mc}}$$

The results in Fig. 8 report $E(r,\varphi)$ corresponding to PC expansion of order $p = 1, 2, 3$. We note that $E(r,\varphi)$ is below 1% for the third-order PC approximation of the pressure field, giving us confidence that the third-order PC expansion provides a sufficiently accurate representation of the uncertain pressure field.

5.1.2 Statistical Analysis of the Pressure Field. In Fig. 9, we depict mean and standard deviation of the pressure field. It is observed that both the value and uncertainty level in pressure is high near the injection site, with diminishing values as we move away from the center; the latter is further illustrated in Fig. 9 (right). From Fig. 9, we also notice that higher levels of pressure uncertainties associate with larger pressure gradients. This indicates that when uncertainties in material properties are propagated into the pressure equation (2), it can induce large uncertainties in the pressure field where there exists large pressure gradients; for regions with small pressure gradients, the induced uncertainties in the pressure field are also small, even though the uncertainty levels of the materials are the same as those in the regions with large pressure gradients.

5.1.3 Variance-Based Sensitivity Analysis. The uncertainty in permeability field, which is modeled as a log-normal processes described earlier, is parameterized by the random vector $\boldsymbol{\xi}$. Here, we perform a global sensitivity analysis to assess the contribution of each of the coordinates of $\boldsymbol{\xi}$ to total variance of the pressure field. This is done by computing the so-called total Sobol indices [33], which we explain briefly here. At a spatial point $\mathbf{x}$, the total-order sensitivity index with respect to the ith input variable ξ_i, denoted by $T_i(\mathbf{x})$, quantifies the total contribution of ξ_i to the variance of $P(\mathbf{x})$. For mathematical definition of the Sobol indices,

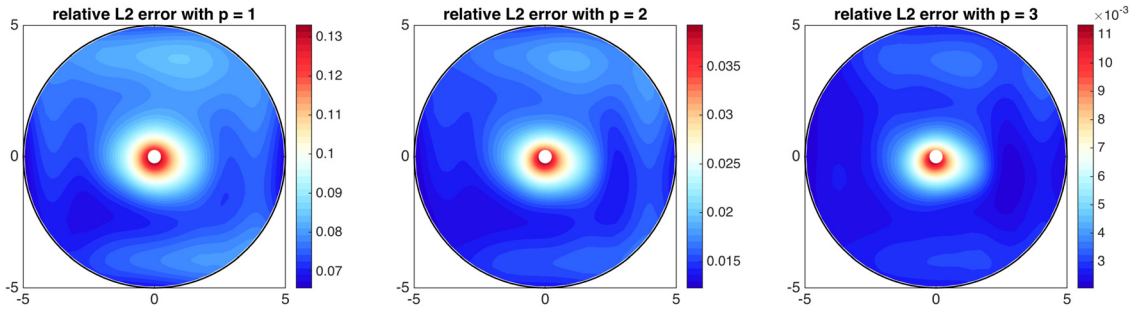

Fig. 8 Computing the relative L_2 error of the PC representation of the pressure field with varying PC order

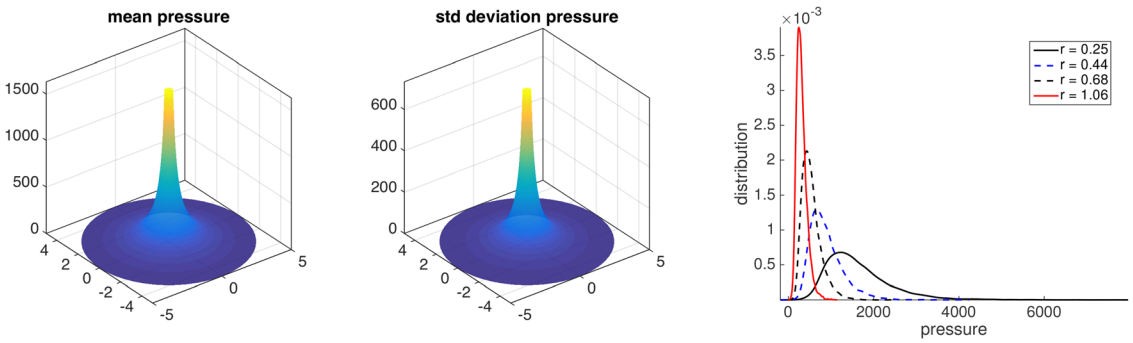

Fig. 9 Mean (left) and standard deviation (middle) of pressure, and distribution of $P(r,\varphi)$ for a fixed φ, and for increasing r (right)

we refer the readers to Refs. [33] and [41]. The computation of Sobol indices using sampling-based methods is generally a difficult problem due to the need for a large number of function evaluations. However, once a PC representation of a random variable is available, computation of Sobol indices can be done at a negligible computational cost [24,34,35]. In particular, given the PC $P(\mathbf{x},\boldsymbol{\xi}) \approx \sum_{k=0}^{N_{PC}} P_k(\mathbf{x})\Psi_k(\boldsymbol{\xi})$, we have

$$T_i(\mathbf{x}) \approx \frac{\sum_{k\in\Lambda_i} P_k(\mathbf{x})^2 ||\Psi_k||^2}{\sum_{k=1}^{N_{PC}} P_k(\mathbf{x})^2 ||\Psi_k||^2}$$

Here, Λ_i is an index set that contains indices of all terms in the PC expansion that contains ξ_i; e.g., see Ref. [24] for details.

In Fig. 10, we report T_i over the physical domain. To facilitate the interpretation of these sensitivity indices, we also consider the following averaged indices: Let T_i be the total sensitivity index due to ξ_i, as mentioned earlier. We can define

$$\bar{T}_i = \frac{1}{|D|}\int_D T_i(\mathbf{x})\, d\mathbf{x}$$

These average indices are summarized in Fig. 11 (left). We also compute the total sensitivity indices for the average pressure at the injection site, defined in Eq. (22). This is reported in Fig. 11 (right).

Based on the presented sensitivity analysis, we make the following observations: (1) The magnitude of the indices for pressure field is small for higher order KL modes. This is seen most easily in Fig. 11 (left) and can be also inferred from the images in Fig. 10. The diminishing contribution of the higher order KL modes to the variability in pressure further justifies the present truncation of KL expansion. (2) The sensitivity analysis results for P^{needle} is interesting; in that, only three KL modes (modes 1, 5, and 9) have notable impact on the variance of this quantity. This clearly shows that for certain observables, the sensitivity indices do not follow the decay of the eigenvalues of the corresponding KL modes. (3) It is interesting, but not surprising, that the first KL mode has the most dominant impact on the variance of the pressure field. All these observations point to the fact that only a subset of KL modes significantly contributes to the uncertainty in the pressure field. From a practical point of view, such information can guide reduction of parameter dimension, which will lead to significant computational saving in the UQ process. Further investigation of such parameter reduction approaches will be the subject of our future work.

5.2 Uncertainty Quantification of the Interstitial Velocity.

Consider the uncertain interstitial velocity defined in Eq. (12). Here, we focus on $v_r = -(\kappa/\phi\mu)(\partial P/\partial r)$. The PC representation of $(\partial P/\partial r)$ along with statistical models for κ and ϕ enables the cheap-to-evaluate approximation

$$v_r(\cdot,\boldsymbol{\xi},\eta) = -\frac{\kappa(\cdot,\boldsymbol{\xi})}{\phi(\eta)\mu}\left(\sum_{k=0}^{N_{PC}} d_k(\cdot)\Psi_k(\boldsymbol{\xi})\right) \tag{23}$$

where $\{d_k(\mathbf{x})\}_{k=0}^{N_{PC}}$ are PC coefficients of $(\partial P/\partial r)$ at a spatial point $\mathbf{x}\in D$, and $\kappa(\mathbf{x},\boldsymbol{\xi})$ and $\phi(\eta)$ are given by Eqs. (9) and (11), respectively. Using this approximation, we can efficiently characterize the statistical properties of v_r. In Fig. 12, we report the mean and standard deviation of v_r in the physical domain, as well as distribution of v_r as we move away from the injection site. The results have been generated by computing Eq. (23) at a Monte Carlo sample $\{(\boldsymbol{\xi}_i,\eta_i)\}_{i=1}^{N}$, with $N = 10^4$. Similar to the random pressure field, it is observed that both the value and variation of

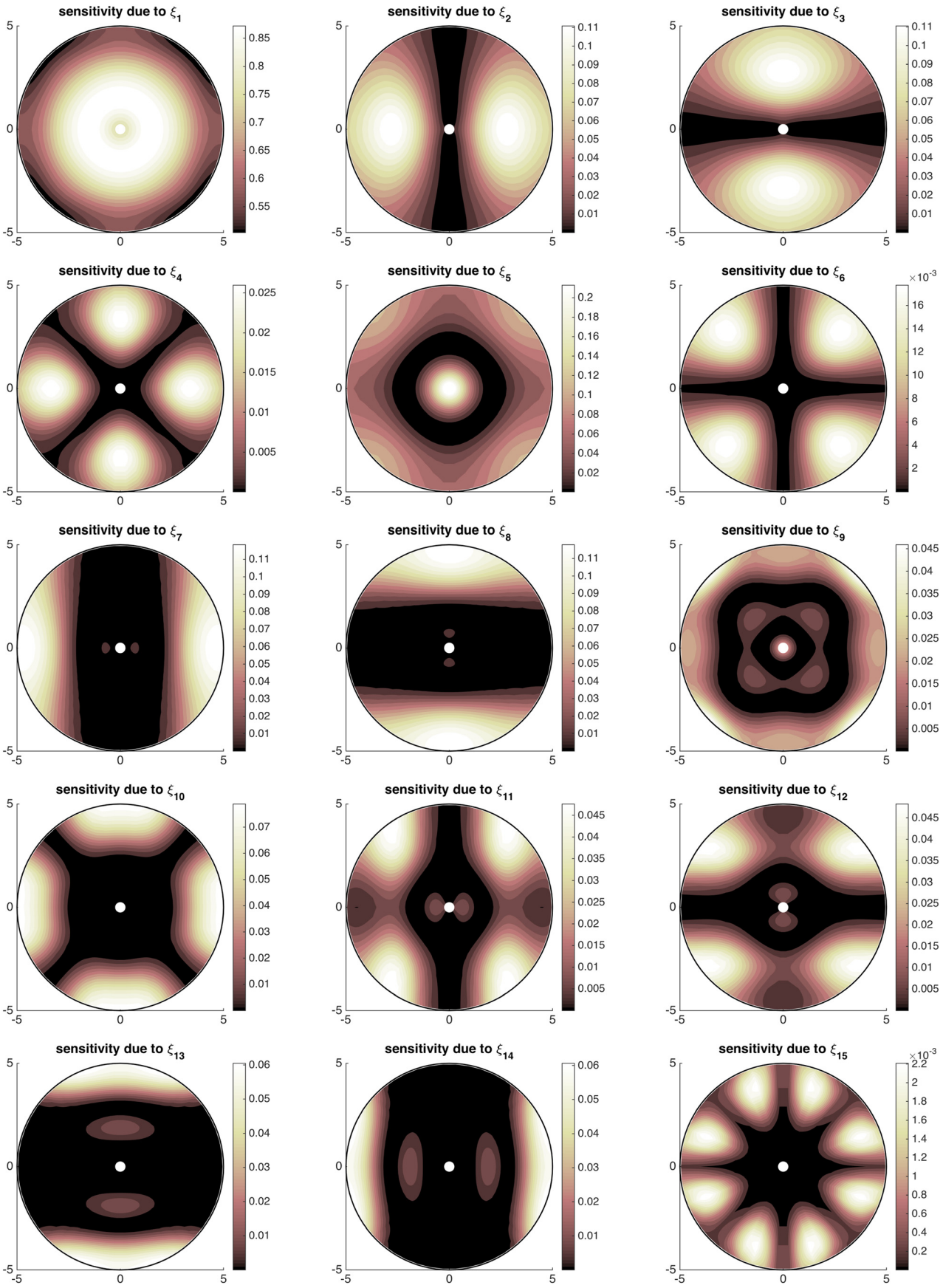

Fig. 10 Total sensitivity indices for the pressure field

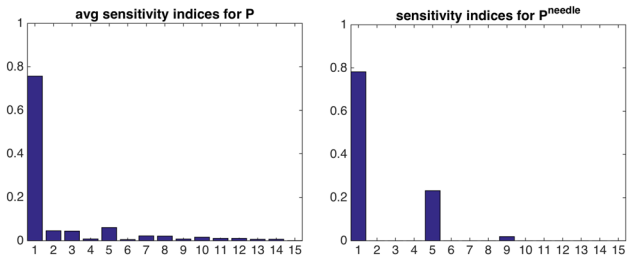

Fig. 11 Average sensitivity indices (left) and sensitivity indices for P^{needle} (right)

the interstitial velocity are high near the injection site, where there exist large velocity gradients.

6 Conclusions

As a long-standing challenge, the distribution of permeability and porosity in a porous tissue is hard to measure or model. We propose to model the uncertain material properties with a statistical approach, in which the permeability is modeled as a random field, and porosity is represented as a random variable. The uncertain nature of the concentration field is visualized from several realizations with random permeability and porosity. The irregularity shown in concentration fields bears reasonable visual agreement with MicroCT scan results.

A nonintrusive spectral uncertainty quantification approach is utilized to assess the uncertainties in flow fields originated from the structural heterogeneity of porous media. To reduce the dimensions in the probability space, a truncated KL expansion is used to represent the uncertain permeability field. The uncertain outputs from the governing partial differential equations are approximated using the PC expansion. A nonintrusive spectral projection approach, using Smolyak sparse quadrature, is used to determine the coefficients of the PC expansion.

The errors in the PC expansion of the random pressure field are examined by comparing the PC results with those from a Monte Carlo sample, as the degree of the PC expansion increases. It is found that the third-order PC expansion provides a sufficiently accurate representation of the random pressure field originated from uncertain permeability. With this PC expansion, the statistics of both the pressure field and the interstitial velocity field is analyzed. It is found that after propagated into the pressure field, the uncertainties in material properties can induce large pressure uncertainties, where there exist large pressure gradients. Similarly, the material uncertainty can induce large uncertainties in the velocity field, where there exist large velocity gradients. In regions with small pressure/velocity gradients, the uncertainties in the pressure/velocity field are also small, even though the uncertainty levels of the materials are the same as those in the regions with large pressure/velocity gradients. A global sensitivity analysis is also performed to assess the contribution of each component of the random vector parameterizing the uncertain permeability field to the total variance of the pressure field. It is found that only certain components significantly contribute to the uncertainty in the pressure field. This information can help further reduce the dimensions of the probability space, thus further decreasing the computational cost of UQ.

We note that in a practical clinical setting, image-based therapy is rising as an invaluable personalized medical tool. Image-based simulation can be used to assist clinical protocol design. However, the computational cost to construct the intratumoral structures and to conduct flow simulation can be huge. Heterogeneous and complex tumor structure and many transport mechanisms involved in nanoparticle spreading in tumors will further make the cost of a high-fidelity image-based simulation prohibitive. Instead, the current study presents a flexible UQ framework to represent and parameterize uncertainties in material properties of tumors and to formulate a porous media flow model that enables efficient computational modeling of biotransport in tumors with quantified uncertainties in model response. Although it is preferable that the distribution of porosity and permeability be derived from experimental data, log-normal distribution used in the present study can serve as a good starting point. The statistical information obtained from the UQ analysis can be used to further improve the clinical protocol designs, e,g., by optimizing drug transport in tumors. We also note that the UQ framework developed here can be adapted to quantify uncertainties in other biotransport systems, e.g., intravenous administration of the nanoparticles in clinical practice.

Acknowledgment

Yu gratefully acknowledges the support from the Department of Mechanical Engineering at University of Maryland, Baltimore County (UMBC), through the faculty startup support.

References

[1] Swartz, M. A., and Fleury, M. E., 2007, "Interstitial Flow and Its Effects in Soft Tissues," Annu. Rev. Biomed. Eng., **9**(1), pp. 229–256.
[2] Debbage, P., 2009, "Targeted Drugs and Nanomedicine: Present and Future," Curr. Pharm. Des., **15**(2), pp. 153–172.
[3] Salloum, M., Ma, R., Weeks, D., and Zhu, L., 2008, "Controlling Nanoparticle Delivery in Magnetic Nanoparticle Hyperthermia for Cancer Treatment: Experimental Study in Agarose Gel," Int. J. Hyperthermia, **24**(4), pp. 337–345.
[4] Hilger, I., Hergt, R., and Kaiser, W., 2005, "Towards Breast Cancer Treatment by Magnetic Heating," J. Mag. Mag. Mater., **293**(1), pp. 314–319.
[5] Rand, R., Snow, H., Elliott, D., and Snyder, M., 1981, "Thermomagnetic Surgery for Cancer," Appl. Biochem. Biotechnol., **6**(4), pp. 265–272.
[6] Rand, R., Snow, H., and Brown, W., 1982, "Thermomagnetic Surgery for Cancer," J. Surg. Res., **33**(3), pp. 177–183.
[7] Hase, M., Sako, M., Fujii, M., Ueda, E., Nagae, T., Shimizu, T., Hirota, S., and Kono, M., 1989, "Experimental Study of Embolo-Hyperthermia for the Treatment of Liver Tumors by Induction Heating to Ferromagnetic Particles Injected Into Tumor Tissue," Nihon Igaku Hoshasen Gakkai Zasshi, **49**(9), pp. 1171–1173.

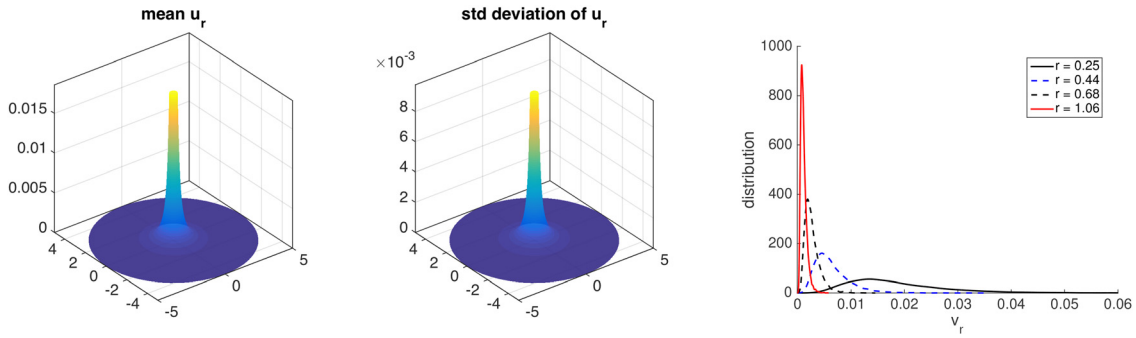

Fig. 12 Mean (left) and standard deviation (middle) of $v_r = -(\kappa/\phi\mu)(\partial P/\partial r)$, and distribution of $v_r(r, \varphi)$ for a fixed φ, and for increasing r (right)

[8] Wust, P., Gneveckow, U., Johannsen, M., Bohmer, D., Henkel, T., Kahmann, F., Sehouli, J., Felix, R., Ricke, J., and Jordan, A., 2006, "Magnetic Nanoparticles for Interstitial Thermotherapy–Feasibility, Tolerance and Achieved Temperatures," Int. J. Hyperthermia, **22**(8), pp. 673–685.
[9] Khaled, A.-R. A., and Vafai, K., 2003, "The Role of Porous Media in Modeling Flow and Heat Transfer in Biological Tissues," Int. J. Heat Mass Transfer, **46**(26), pp. 4989–5003.
[10] Baxter, L. T., and Jain, R. K., 1990, "Transport of Fluid and Macromolecules in Tumors (II): Role of Heterogeneous Perfusion and Lymphatics," Microvasc. Res., **40**(2), pp. 246–263.
[11] Wang, C.-H., and Li, J., 1998, "Three-Dimensional Simulation of IgG Delivery to Tumors," Chem. Eng. Sci., **53**(20), pp. 3579–3600.
[12] Zhao, J., Salmon, H., and Sarntinoranont, M., 2007, "Effect of Heterogeneous Vasculature on Interstitial Transport Within a Solid Tumor," Microvasc. Res., **73**(3), pp. 224–236.
[13] Pishko, G. L., Astary, G. W., Mareci, T. H., and Sarntinoranont, M., 2011, "Sensitivity Analysis of an Image-Based Solid Tumor Computational Model With Heterogeneous Vasculature and Porosity," Ann. Biomed. Eng., **39**(9), pp. 2360–2373.
[14] Sefidgar, M., Soltani, M., Raahemifar, K., Bazmara, H., Nayinian, S. M. M., and Bazargan, M., 2014, "Effect of Tumor Shape, Size, and Tissue Transport Properties on Drug Delivery to Solid Tumors," J. Biol. Eng., **8**(1), p. 12.
[15] Xiu, D., Lucor, D., Su, C., and Karniadakis, G., 2002, "Stochastic Modeling of Flow Structure Interactions Using Generalized Polynomial Chaos," ASME J. Fluids Eng., **124**(1), pp. 51–59.
[16] Xiu, D., and Karniadakis, G., 2002, "The Wiener-Askey Polynomial Chaos for Stochastic Differential Equations," SIAM J. Sci. Comput., **24**(2), pp. 619–644.
[17] Xiu, D., and Karniadakis, G., 2003, "Modeling Uncertainty in Flow Simulations Via Generalized Polynomial Chaos," J. Comput. Phys., **187**(1), pp. 137–167.
[18] Le Maître, O., Knio, O., Najm, H., and Ghanem, R., 2004, "Uncertainty Propagation Using Wiener-Haar Expansions," J. Comput. Phys., **197**(1), pp. 28–57.
[19] Le Maître, O., Najm, H., Ghanem, R., and Knio, O., 2004, "Multi-Resolution Analysis of Wiener-Type Uncertainty Propagation Schemes," J. Comput. Phys., **197**(2), pp. 502–531.
[20] Le Maître, O., Mathelin, L., Knio, O., and Hussaini, M., 2010, "Asynchronous Time Integration for Polynomial Chaos Expansion of Uncertain Periodic Dynamics," Discrete Contin. Dyn. Syst., **28**(1), pp. 199–226.
[21] Le Maître, O. P., and Knio, O. M., 2010, *Spectral Methods for Uncertainty Quantification*: *With Applications to Computational Fluid Dynamics*, Springer, New York.
[22] Hosder, S., Walters, R., and Perez, R., 2006, "A Non-Intrusive Polynomial Chaos Method for Uncertainty Propagation in CFD Simulations," AIAA Paper No. 2006-891.
[23] Babuška, I., Nobile, F., and Tempone, R., 2007, "A Stochastic Collocation Method for Elliptic Partial Differential Equations With Random Input Data," SIAM J. Numer. Anal., **45**(3), pp. 1005–1034.
[24] Alexanderian, A., Winokur, J., Sraj, I., Srinivasan, A., Iskandarani, M., Thacker, W., and Knio, O., 2012, "Global Sensitivity Analysis in Ocean Global Circulation Models: A Sparse Spectral Projection Approach," Comput. Geosci., **16**(3), pp. 757–778.
[25] Smolyak, S. A., 1963, "Quadrature and Interpolation Formulas for Tensor Products of Certain Classes of Functions," Dokl. Akad. Nauk SSSR, **4**, pp. 240–243.
[26] Liu, J., 2001, "Uncertainty Analysis for Temperature Prediction of Biological Bodies Subject to Randomly Spatial Heating," J. Biomech., **34**(12), pp. 1637–1642.
[27] Rabin, Y., 2003, "A General Model for the Propagation of Uncertainty in Measurements Into Heat Transfer Simulations and Its Application to Cryosurgery," Cryobiology, **46**(2), pp. 109–120.
[28] Turner, T. E., Schnell, S., and Burrage, K., 2004, "Stochastic Approaches for Modelling In Vivo Reactions," Comput. Biol. Chem., **28**(3), pp. 165–178.
[29] Deng, Z.-S., and Liu, J., 2002, "Monte Carlo Method to Solve Multidimensional Bioheat Transfer Problem," Numer. Heat Transfer, Part B, **42**(6), pp. 543–567.
[30] Ghanem, R., and Dham, S., 1998, "Stochastic Finite Element Analysis for Multiphase Flow in Heterogeneous Porous Media," Transp. Porous Media, **32**(3), pp. 239–262.
[31] Saad, G., and Ghanem, R., 2009, "Characterization of Reservoir Simulation Models Using a Polynomial Chaos-Based Ensemble Kalman Filter," Water Resour. Res., **45**(4), p. W04417.
[32] Sobol, I., 2001, "Global Sensitivity Indices for Nonlinear Mathematical Models and Their Monte Carlo Estimates," Math. Comput. Simul., **55**(1–3), pp. 271–280.
[33] Sobol, I., 1990, "On Sensitivity Estimation for Nonlinear Mathematical Models," Mat. Model., **2**(1), pp. 112–118.
[34] Sudret, B., 2008, "Global Sensitivity Analysis Using Polynomial Chaos Expansions," Reliab. Eng. Syst. Saf., **93**(7), pp. 964–979.
[35] Crestaux, T., Maitre, O. L., and Martinez, J.-M., 2009, "Polynomial Chaos Expansion for Sensitivity Analysis," Reliab. Eng. Syst. Saf., **94**(7), pp. 1161–1172.
[36] Ma, R., Su, D., and Zhu, L., 2012, "Multiscale Simulation of Nanopartical Transport in Deformable Tissue During an Infusion Process in Hyperthermia Treatments of Cancers," *Nanoparticle Heat Transfer and Fluid Flow* (Computational and Physical Processes in Mechanics and Thermal Science Series), Vol. 4, W. J. Minkowycz, E. Sparrow, and J. P. Abraham, eds., CRC Press, Boca Raton, FL.
[37] Ghanem, R. G., and Spanos, P. D., 1991, *Stochastic Finite Elements: A Spectral Approach*, Springer-Verlag, New York.
[38] Mercer, J., 1909, "Functions of Positive and Negative Type, and Their Connection With the Theory of Integral Equations," Philos. Trans. R. Soc. London Ser. A, **209**(441–458), pp. 415–446.
[39] Xiu, D. B., 2010, *Numerical Methods for Stochastic Computations*, Princeton University Press, Princeton, NJ.
[40] Heiss, F., and Winschel, V., 2008, "Likelihood Approximation by Numerical Integration on Sparse Grids," J. Econometrics, **144**(1), pp. 62–80.
[41] Sobol, I., Tarantola, S., Gatelli, D., Kucherenko, S., and Mauntz, W., 2007, "Estimating the Approximation Error When Fixing Unessential Factors in Global Sensitivity Analysis," Reliab. Eng. Syst. Saf., **92**(7), pp. 957–960.